2018

Construction of Hierarchical MoSe2 Hollow Structures and Its Effecton Electrochemical Energy Storage and Conversion

Sha Hu
South-Central University For Nationalities

Qingqing Jiang
South-Central University For Nationalities

Shuoping Ding
South-Central University For Nationalities

Ye Liu
South-Central University For Nationalities

Zuozuo Wu
South-Central University For Nationalities

See next page for additional authors

Publication Details

Hu, S., Jiang, Q., Ding, S., Liu, Y., Wu, Z., Huang, Z., Zhou, T., Guo, Z. & Hu, J. (2018). Construction of Hierarchical MoSe2 Hollow Structures and Its Effecton Electrochemical Energy Storage and Conversion. Acs Applied Materials & Interfaces, 10 (30), 25483-25492.

Construction of Hierarchical MoSe2 Hollow Structures and Its Effecton Electrochemical Energy Storage and Conversion

Abstract
Metal selenides have attracted increased attentionas promising electrode materials for electrochemical energy storageand conversion systems including metal-ion batteries and watersplitting. However, their practical application is greatly hindered bycollapse of the microstructure, thus leading to performance fading.Tuning the structure at nanoscale of these materials is an effectivestrategy to address the issue. Herein, we craft MoSe2withhierarchical hollow structures via a facile bubble-assistedsolvothermal method. The temperature-related variations of thehollow interiors are studied, which can be presented as solid, yolk−shell, and hollow spheres, respectively. Under the simultaneousaction of the distinctive hollow structures and interconnectionsamong the nanosheets, more intimate contacts between MoSe2and electrolyte can be achieved, thereby leading to superior electrochemical properties. Consequently, the MoSe2hollownanospheres prepared under optimum conditions exhibit optimal electrochemical activities, which hold an initial specificcapacity of 1287 mA h g−1and maintain great capacity even after 100 cycles as anode for Li-ion battery. Moreover, the Tafelslope of 58.9 mV dec−1for hydrogen evolution reaction is also attained.

Keywords
structures, hollow, mose2, hierarchical, construction, conversion, energy, storage, electrochemical, effecton, its

Disciplines
Engineering | Physical Sciences and Mathematics

Publication Details
Hu, S., Jiang, Q., Ding, S., Liu, Y., Wu, Z., Huang, Z., Zhou, T., Guo, Z. & Hu, J. (2018). Construction of Hierarchical MoSe2 Hollow Structures and Its Effecton Electrochemical Energy Storage and Conversion. Acs Applied Materials & Interfaces, 10 (30), 25483-25492.

Authors
Sha Hu, Qingqing Jiang, Shuoping Ding, Ye Liu, Zuozuo Wu, Zhengxi Huang, Tengfei Zhou, Zaiping Guo, and Juncheng Hu

Construction of Hierarchical $MoSe_2$ Hollow Structures and Its Effect on Electrochemical Energy Storage and Conversion

Sha Hu [a, #], Qingqing Jiang [a, #], Shuoping Ding [a], Ye Liu [a], Zuozuo Wu [a], Zhengxi Huang [a], Tengfei Zhou [a,b,c] *, Zaiping Guo [b], Juncheng Hu [a,*]

a Key Laboratory of Catalysis and Materials Science of the State Ethnic Affairs Commission & Ministry of Education, Hubei Province, South-central University for Nationalities, Wuhan 430074, P. R. China

b Institute for Superconducting & Electronic Materials, School of Mechanical, Materials, Mechatronics & Biomedical Engineering, Faculty of Engineering and Information Sciences, University of Wollongong, Wollongong, NSW 2500, Australia

c Key Laboratory of Advanced Energy Materials Chemistry (Ministry of Education), Nankai University, Tianjin 300071, China.

[#] S. Hu and Q. Jiang contributed equally to this work.

To whom correspondence should be addressed. Email: jchu@mail.scuec.edu.cn, tfzhou@scuec.edu.cn

ABSTRACT

Metal selenides have attracted increased attention as promising electrode materials for electrochemical energy storage and conversion systems including metal-ion batteries and water splitting. However, their practical application is greatly hindered by collapse of the microstructure and thus leading to performance fading. Tuning the structure at nanoscale of these materials is an effective strategy to address the issue. Herein, we craft $MoSe_2$ with hierarchical hollow structures via a facile bubble-assisted solvothermal method. The temperature-related variations of the hollow interiors are studied, which can be presented as solid, yolk-shell and hollow spheres, respectively. Under the simultaneous action of the distinctive hollow structures and interconnections among the nanosheets, more intimate contacts between $MoSe_2$ and electrolyte can be achieved, whereby leading to superior electrochemical properties. Consequently, the $MoSe_2$ hollow nanospheres prepared under optimum conditions exhibit the optimal electrochemical activities, which hold an initial specific capacity of 1287 mA h g^{-1} and maintain great capacity even after 100 cycles as anode for Li-ion battery. Moreover, the Tafel slope of 59 mV dec^{-1} for hydrogen evolution reaction is also attained.

KEYWORDS: $MoSe_2$, hollow structures, ultrathin nanosheets, LIBs, HER

1. INTRODUCTION

Triggered by the infinite consumption of fossil fuels, the increasingly serious environmental issues and energy crisis have stimulated the urgent demand of sustainable energy tactics, in which developing clean energy vectors and high-performance energy storage medium are the foremost topics.[1, 2] Lithium-ion batteries attracted great attention for the high energy ratio, long service life and high rated voltage in renewable energy storage system. Meanwhile, electrocatalytic water splitting to hydrogen is also considered as one of the most effective way to generate the clean H_2 energy.[3, 4] Efforts have been dedicated to search for the candidate materials used in both energy production and storage. Benefit from the abundant reserves on earth, transition metal dichalcogenides (TMDs) MX_2 (M=Mo, W; X=S, Se, Te) could be considered as promising candidates, in which $MoSe_2$ has been widely studied among researchers for its excellent chemical properties.[5-8] The graphite-like Se-Mo-Se sandwich layered structure in $MoSe_2$ is sustained by weak Van der Waals force, and the sufficient spacing with an interlayer distance of 0.65 nm enables more efficient Li^+ insertion and extraction, which could be potentially used as LIBs anodes.[9, 10] Considering the low theoretical capacity of graphite anode material (372 mA h g^{-1}), the high theoretical capacity of $MoSe_2$ (422 mA h g^{-1}) is also a considerable advantage when used as anode materials.[11] Furthermore, both calculative and experimental results proved that all the molybdenum and selenium edge sites are active for hydrogen evolution reaction (HER), which makes $MoSe_2$ a promising electrocatalyst for HER.[12] Nevertheless, the practical application of $MoSe_2$ is still largely restricted by intrinsic limitations, such as pronounced volume variation for LIBs and insufficient electrochemical active sites for the HER, respectively.[13, 14]

To solve these problems, various strategies including nano-sizing, element coating and building heterostructures have been employed to optimize the performance of $MoSe_2$.[15-16] In virtue of the internal void space, large specific surface area, curtate diffusion distance of ions and mitigatory change of the electrode volume, engineering hollow structures is a better means compared to the above strategies.[17,18] The most common tactic to design nanoscale

hollow sphere depends on hard or soft templates. However, difficulties are often encountered in forming solid shells with the ideal composition and effectively removing the templates. The gas bubble-assisted synthesis is an effective route to prepare hollow spheres without the issues caused by templates.[19] For instance, Wang and his team synthesized ZnO hollow spheres with double-yolk egg structure with N_2 flows.[20] Li et al. also reported ZnSe hollow spheres by using N_2 as the soft template, during which N_2 bubbles were released from the reducing agent citric acid.[17] Inspired by these previous works, it is very effective to design $MoSe_2$ hollow spheres through a gas bubble-assisted approach.

In this work, we present the controllable synthesis of $MoSe_2$ nanospheres with different hollow interiors via a facile in situ gas bubble-templated method. In our work, $N_2H_4 \cdot H_2O$ would work as not only the reductant but also the source of N_2 bubbles, which is a key to formation of cavity, while the reaction temperature plays the essential roles in the modulation of the interiors including solid, yolk-shell and hollow nanospheres. In virtue of the unique hollow structure and interconnections of the ultrathin nanosheets, the hierarchical $MoSe_2$ hollow nanospheres prepared in this work exhibit high initial specific capacity toward LIBs, and still maintain excellent capacity after 100 cycles. And low overpotential, excellent stability for electrochemical HER are also achieved. This work may offer a new way toward the optimization of selenium-based nanomaterials for energy-related electrochemical applications.

2. EXPERIMENTAL SECTION

2.1. Chemicals and Materials

Ammonium molybdate hydrate ($(NH_4)_6Mo_7O_{24} \cdot 4H_2O$), hydrazine hydrate ($N_2H_4 \cdot H_2O$, 85%), selenium powder (Se), ethylenediamine (EDA) and ethanol were provided by Sinopharm Chemical Reagent Co, Ltd. molybdenum trioxide (MoO_3) was purchased from Aladdin.

2.2. Synthesis of 1D MoO_x-EDA

In a typical process, 0.8g ammonium molybdate hydrate was dispersed in 30 mL ethylenediamine in a 100 mL autoclave under vigorous stirring for 0.5h, and then hydrothermally treated at 180 ℃ for 8 h. After cooling down naturally, the precipitate was filtrated and washed with ethanol for four times. Finally, the obtained powders were dried and collected at 55℃ for 12 hours in a vacuum oven. The final products were denoted as MoO_x-EDA.

2.3. Synthesis of $MoSe_2$ with Different Hollow Structures

In a typical process, 30 mg Se powder and 30mg MoO_3 powder were dispersed in 5mL of N_2H_4•H_2O solution. Then, 10 mL distilled water and 15 mL ethanol were added under stirring for 10 min. Subsequently, 21.4 mg MoO_x-EDA was added with next 20 min stirring. After that, the mixture was transferred to a 100 mL autoclave for solvothermal treatment at different temperatures (100 ℃, 140 ℃, 180 ℃, 220 ℃) for 6h. After cooling down, the precipitate was washed with ethanol for 5 times, and then dried at 60 ℃. $MoSe_2$ nanospheres prepared under different temperatures (100℃, 140℃, 180℃ and 220℃) were denoted as MSS for solid spheres, MYS for yolk-shell nanospheres, MHS-1 and MHS-2 for hollow nanospheres.

Detailed characterizations and electrochemical measurements can be found in the Supporting Information.

3. RESULTS and DISCUSSION

3.1. Characterization of Structure and Morphology

The morphologies and microstructures of the $MoSe_2$ nanospheres were characterized by SEM and TEM. (**Figure 1**). Specifically, solid, yolk-shell and hollow nanospheres can be readily obtained by simply varying the reaction temperature. As illustrated in Figure 1a and 1e, when the synthesis temperature is 100 ℃, the as-synthesized $MoSe_2$ are uniform solid nanospheres (MSS) with an average size of ~400 nm, which are composed of ultrafine interconnected nanoparticles. As the temperature increased to 140 ℃, $MoSe_2$ samples exhibited yolk–shell structure (MYS), and the nanospheres are evenly coated by some shallow nanosheets (Figure 1b). The TEM image further confirms the features of the yolk–shell structure: a distinct core and a clear gap between the core and shell,

which could be observed clearly in Figure 1f. Interestingly, when it comes to the $MoSe_2$ product synthesized at 180 °C, the hollow structures and well-defined inner cavities are distinctly illustrated (MHS-1), and the surface is a superstructure assembled by numerous interconnected ultrathin nanosheets with thickness of about 3.5 nm, which could be confirmed by HRTEM. The representative HRTEM image (Figure S1) of MHS-1 illustrates the layered crystal lattice structure and the spacings of 0.67 nm correspond to the interlayer distance of (002) plane of the hexagonal $MoSe_2$ phase.[6] When the solvothermal temperature increased to 220 °C, the hierarchical nanospheres still showed hollow structures, while the nanosheet subunits of these hierarchical nanospheres became larger and thicker (Figure 1d, 1h).

Figure 2 depicts the XRD patterns of the as synthesized $MoSe_2$ at different reaction temperatures. The samples synthesized at 100 °C and 140 °C exhibited the amorphous characteristics. As the reaction temperature increased to 180 °C and 220 °C, two major peaks at 33.17° and 55.41° corresponding to (100) and (110) planes were observed clearly.[21] These diffraction peaks are in good consistence with the standard pattern (JCPDS card, no. 29-0914), suggesting that hexagonal $MoSe_2$ is successfully prepared in our experiment. The broad diffraction peaks indicate the poor crystallinity of the as-prepared $MoSe_2$, no impurities are detected, which further confirms the high purity of the samples. Besides, the formation of two-dimensional hexagonal array (2H-$MoSe_2$) can be further confirmed by Raman spectroscopy with the excitation laser line at 532 nm (**Figure 3a**). The characteristic signatures of Raman peaks at 166.88, 239.74, and 283.75 cm^{-1} are attributed to the E_{1g}, A_{1g}, and $E_{2g}{}^1$ modes of 2H-MoSe2, respectively.[22, 23]

Raman and PL spectrum were further utilized to implement the thickness variations of $MoSe_2$ nanosheets at larger length scales.[22, 23] Figure 3a indicates the temperature-dependent evolution of the thickness of the nanosheets. The most identifiable peak located at 244 cm^{-1} is A_{1g} mode for bulk $MoSe_2$ and the shift of A_{1g} mode is mainly attributed to the changes in the thickness of nanosheets. [24] The peak of PL spectra shown in Figure 3b located at ~

755 nm corresponds to a band gap of 1.64 eV and agrees well with previous reported 1.4-1.6 eV for $MoSe_2$ nanosheets. [25] With the reaction temperature increases, the intensity of the peak augments, which also implies an increase in the thickness of the nanosheets of $MoSe_2$ samples.

X-ray photoelectron spectroscopy (XPS) analysis was employed to reveal the chemical compositions and chemical state of the element of $MoSe_2$. The Mo 3d XPS spectrum displays two peaks at approximately 228.6 and 231.1 eV, which are corresponding to Mo $3d_{3/2}$ and Mo $3d_{5/2}$ of Mo (IV) state in $MoSe_2$, respectively, and they are similar to the positions for MoS_2 and $MoSe_2$-based systems in previous reports.[26] The peaks at 232.1 and 235.7 eV belonged to Mo (VI) in residual MoO_3.[27] The Se 3d spectrum can be divided into Se $3d_{5/2}$ and Se $3d_{3/2}$ with peak positions at approximately 54.1 and 55.2 eV, respectively, which are assigned to the -2 oxidation state of Se in $MoSe_2$. [28]

3.2. Formation Mechanism of Hollow Structures

Based on these observations, an aggregation mechanism for the formation of hollow $MoSe_2$ spheres is proposed. The formation mechanism of the present structures was assigned to the bubble-assisted method along with Ostwald ripening process, with reference to the preparation of monodispersed ZnSe or ZnO hollow microspheres.[17,20] In our reactions, when $N_2H_4 \cdot H_2O$ was added to the reaction system, $N_2H_4 \cdot H_2O$ would work as not only the reductant to reduce MoO_3 and Se to Mo^{4+} ions and Se^{2-} ions, respectively, but also the source of N_2 bubbles.[20] Upon the MoO_x-EDA precursor dissolved in the $N_2H_4 \cdot H_2O$ solution, Mo^{4+} ions are further formed and NH_3 arised.[29,30] When the reaction temperature is 100°C, the gas will not be released due to the low temperature. After Mo^{4+} ions and Se^{2-} ions reacted to form $MoSe_2$ small nanocrystals, these monomers would aggregate together to form 3D microspheres driven by the minimization of the system energy.[20] Upon the reaction temperature arrived at 140°C, the increased temperature speeded up the reaction rate. The N_2 and NH_3 bubbles were gradually released, some bubbles adsorbed at the surface of the growing nanospheres (inner spheres), other $MoSe_2$ nanocrystals aggregated around the bubbles

to form the shells, thus, the yolk-shell spheres (MYS) formed. At the same time, some shallow sheets appeared at the surface of shell, as illustrated in Scheme 1. With the reaction temperature increasing to 180°C, the rate of reaction was further accelerated, lots of N_2 and NH_3 bubbles were released before $MoSe_2$ nanocrystals aggregated, and these bubbles provided the aggregation center, small $MoSe_2$ nanocrystals would aggregate around the gas-liquid interface between bubbles and H_2O, leading to the formation of $MoSe_2$ hollow spheres.[17] Meanwhile, due to the Ostwald ripening effect, smaller-sized nanocrystals would dissolve to form larger nanosheets, plentiful large sized ultrathin nanosheets appeared at the surface of $MoSe_2$ hollow spheres. Thus, the $MoSe_2$ hollow nanospheres (MHS-1) formed (Scheme 1). Finally, when the sample prepared at 220 °C, the reaction rate is higher than that under the 180 °C condition, resulting in the thicker and larger of the crystalline nanosheets, while the hollow structure of $MoSe_2$ nanospheres (MHS-2) is nearly unchanged, compared to MHS-1.

Generally, the above phenomena proved that the reaction temperature has a significant effect on the internal structure of $MoSe_2$ nanospheres. Alternatively, the increased temperature accelerated the velocity of gas release, aggregation process, the small crystals dissolution, and the large crystals formation. Thus, the structure of the internal cavity and the size of the nanosheets differ greatly with the aggrandized temperature.

3.3. BET Analysis

The nitrogen adsorption-desorption isotherms of MHS-1 was shown in Figure S2. As shown in **Table 1**, the BET surface areas of these samples are 2.1 $m^2\ g^{-1}$ for MSS, 17.9 $m^2\ g^{-1}$ for MYS, 66.5 $m^2\ g^{-1}$ for MHS-1 and 41.9 $m^2\ g^{-1}$ for MHS-2, respectively. To the best of our knowledge, $MoSe_2$ samples in our experiments have higher surface area than previously reported works.[6, 17] It is generally acknowledged that materials with a high specific surface area could have more active sites and the distribution of active sites is more uniform. Taking it into consideration, we surmise that the hollow nanospheres with higher BET surface area could enhance the electrocatalytic activity.

3.4. Electrochemical Performance for LIBs

The $MoSe_2$ nanospheres were explored as the anodes for LIBs to exhibit their preeminent application. **Figure 4**a displays the CV curves of MHS-1 electrode for the first three cycles, which ran in a voltage range of 0.01–3.0 V at 0.1 mV s^{-1}. The multipeak features of the CV curves demonstrates that the reaction of the $MoSe_2$ hollow nanosphere is a multi-step process. In the first cycle, the discharge peaks are located at 1.62 V, 1.20 V and 0.59 V, while the charge peaks at 1.96 V and 2.23 V. The reductive peak at 1.62 V relates to the insertion of Li into the layered structure of the $MoSe_2$ hollow nanosphere to form Li_xMoSe_2.[31] The cathodic peak at 1.20 V and 0.59 V indicates the reduction of Li_xMoSe_2 to Mo and $LiSe_2$, simultaneously, the solid electrolyte interface (SEI) film formed.[32] In the oxidation cycle, two peaks located at 1.96 V and 2.23 V corresponding to the conversion reaction of Li_2Se and Mo to $MoSe_2$, respectively. In the following profiles, the anodic peak at 0.59 V disappears, and generally shifted to a higher voltage at 1.82 V and 1.23 V, respectively, while the oxidation peaks remained at 1.96 V and 2.23 V. Importantly, both the reductive and oxidative peaks in the CV profiles overlap well, demonstrating the excellent stability and reversibility of the MHS-1 electrode.

The galvanostatic discharge-charge curves of $MoSe_2$ for the selected cycles (1st, 2nd, 10th, 50th and 70th) at a current density of 100 mA g^{-1} are showed in Figure 4b. A high discharge capacity of 1287 mA h g^{-1} is surveyed at the first discharge with an initial irreversible loss of about 32%. The low initial coulombic efficiency (CE) is mainly gave rise to the formation of the SEI film and degradation of electrolyte at the interface between the electrolyte and the electrode.[33]

Comparative cyclic behaviors of different $MoSe_2$ electrodes were investigated under a current density of 100 mA h g^{-1} (Figure 4c). It is obvious that MHS-1 shows the optimal cycling stability among the samples. The specific discharge capacity of MHS-1 gradually increased after the 2nd cycle and reached 1435 mA h g^{-1} after 100th cycles with a coulombic efficiency of ≈ 100%. In comparison, the MSS exhibits poor cycling stability with the continuous decreasing cyclic performance and the cyclic performances of MYS and MHS-2 are evident weaker than MHS-1.

To further investigate the electrochemical performances of $MoSe_2$ electrodes, the rate capabilities of both samples were compared. Figure 4d demonstrates the rate capability of four $MoSe_2$ electrodes at an increasing rate of 100, 200, 500, 1000, 2000 and 5000 mA g^{-1}. As can be seen clearly, the MHS-1 manifests outstanding high-rate performance. The specific capacities of the MHS-1 electrode are nearly 621 and 502 mA h g^{-1} at the current densities of 2000 and 5000 mA g^{-1}, respectively, which are much higher than for the MSS, MYS, and MHS-2. The long-range cycling performance of the MHS-1 electrode is showed in Figure 4e. A high discharge capacity of 652 mA h g^{-1} is immediately resumed after 500 cycles at 1000 mA g^{-1} (≈86% capacity retention), suggesting the eminent cycling stability.

The lithium-ion diffusion coefficient (D_{Li+}) can be calculated on the basis of the Randles-Sevcik Equation: $i_p = (2.69 \times 10^5) n^{3/2} S D^{1/2} C v^{1/2}$ (1). Since the prepared and tested routine of the two electrodes are the same, the Randles-Sevchik equation can be further simplified as: $i_p = A v^{1/2}$ (2), in which A is considered as the apparent Li^+ diffusion coefficient in the cells and can be calculated by fitting the linear curves in Figure 5. Speculated from the results, the apparent Li^+ diffusion coefficient of MHS-1 is much higher than that of MSS.

To gain further insights into the electrochemical behaviors of the $MoSe_2$ electrode, the EIS measurements was conducted. As shown in Figure S3, each sample exhibits a semicircle in the high frequency region and an oblique line in the low frequency region. Generally, the charge transfer resistance of the interface between the electrode and electrolyte could be inferred from the diameter of the semicircles. In this regard, MHS-1 possesses lower contact and charge transfer resistances, as the diameter of the semicircle in high frequency region for MHS-1 electrodes is smaller than other $MoSe_2$ electrodes.

Stable cycling of an electrode has strict requirements in terms of structural stability at the particle level. The surface morphologies of electrodes were investigated at the same cycling stages via SEM. No obvious cracks can be observed for the MHS-1 electrode after cycling, whereas others showed microcracks over the electrode surface

(Figure 6 a1-d1 and a2-d2), suggesting that MHS-1 electrode has the highest mechanical capability to tolerate the stress during charge–discharge cycling. $MoSe_2$ electrodes before (a3-d3) and after (a4-d4) 10 cycles at the current density of 200 mA g^{-1} was examined with SEM and there is no obvious structural change after cycling. As the SEM micrographs in Figure 6 demonstrate, we can see a thin solid electrolyte interphase (SEI) film on the sample surface after 10 cycles.

The optimal LIBs performance originates from the following factors: (1) High-density interconnected ultrathin $MoSe_2$ nanosheets are conducive to accommodate Li ions with lower diffusion resistance and increase the capacity for Li ions. (2) Hollow nanostructure with large surface area provides sufficient area for contact between electrolyte and anode material and reduces the distance for ions intercalation/de-intercalation. (3) The internal void space makes for maintaining the stability of the electrode structures when accommodating large volume changes caused by electrochemical reactions. Therefore, the outstanding LIBs performance of $MoSe_2$ hollow nanospheres is attributed to the high-density interconnected ultrathin nanosheets, together with large surface area and internal void space of the unique hollow structure.

3.5. HER Reaction

The HER electrocatalytic activities of the $MoSe_2$ products are measured in a 0.5 M H_2SO_4 electrolyte by applying a standard three-electrode configuration. The polarization curves (**Figure 7**a) shows that MHS-1 electrode exhibits the onset overpotential of 150 mV (vs RHE). The onset overpotential of MSS, MYS, and MHS-2 is 200 mV, 190 mV and 170 mV, respectively. As a comparison, pure bulk $MoSe_2$ shows onset overpotential above 200 mV (vs RHE). The MHS-1 electrode required a low overpotential of 242 mV at the cathodic current density of 10 mA cm^{-2}.

The Tafel slope (Figure 7b) derived from the polarization curves is directly related to the rate-determining step in the whole HER process.[36] The Tafel slopes measured from these $MoSe_2$-based samples are in the range of 59-102

mV dec^{-1} which is smaller than bulk $MoSe_2$ (120-190 mV dec^{-1}). Among them, the MHS-1 show the lowest Tafel slope of 59 mV per decade, which indicates its fastest reaction kinetics. In addition, the Tafel slope is also applied to distinguish the pathways in the HER process in acidic electrolyte. According to previous publications, there are three possible reaction steps for the HER in acidic aqueous.

$$\text{Volmer step: } H^+ + e^- + \text{cat} \rightarrow H_{ads}\text{-cat} + H_2O \quad (1)$$

$$\text{Heyrovsky step: } H_{ads}\text{-cat} + H^+ + e^- \rightarrow H_2 + H_2O \quad (2)$$

$$\text{Tafel step: } H_{ads}\text{-cat} + H_{ads}\text{-cat} \rightarrow H_2 \quad (3)$$

Volmer is the rate-determining step in HER reaction at a Tafel slopes of about 120 mV dec^{-1}, and Heyrovsky or Tafel reaction is the rate-limiting procedure when Tafel slopes in the range of 30 mV dec^{-1} and 40 mV dec^{-1}. The Tafel slopes measured from these $MoSe_2$ products are in the range of 59-102 mV dec^{-1} which suggests that the rate-determining step on our $MoSe_2$ catalysts may be the Volmer-Heyrovsky or Volmer-Tafel mechanism.[36-37]

The charge transfer resistances are also essential factors for high HER electrocatalysis activity except for more active HER catalysis sites.[37] Figure 7d displays the electrochemical impedance spectroscopy tests at an overpotential of 180 mV. The lower charge transfer resistance means a faster electron transfer at the interface between electrocatalysts and electrolytes. Among these $MoSe_2$ samples, the MHS-1 exhibited the lowest charge transfer impedance which indicates faster electrode kinetics during HER reaction.

Furthermore, the long-term stability is another significant parameter of the electrocatalysts.[38] As exhibited in Figure 6c, the cathodic current density displays a negligible degradation after a period of 18000 s under the operation of overpotential of 230 mV, indicating the excellent durability of MHS-1 toward HER. The MHS-1 exhibited the best HER performance than other samples due to its internal void space, large ultrathin interconnect nanosheets, large surface-to-volume ratio and high porosity. These results are well coincident with the performances of LIBs.

4. CONCLUSIONS

In summary, we demonstrate the approach of $MoSe_2$ hollow nanospheres via a facile in-situ gas bubble assisted solvothermal route. Under the synergetic effect of the ultrathin nanosheets and the unique structural advantages of hollow spheres, the electrochemical performances of $MoSe_2$ products were greatly enhanced. As a consequence, $MoSe_2$ hollow nanospheres exhibited a high reversible capacity of 1435 mA g^{-1} even after 100 cycles as LIBs anode. Moreover, the onset potential and Tafel slope of $MoSe_2$ hollow nanospheres were lowered to 150 mV and 59 mV dec^{-1} and owned a long-term stability for HER. It is worth mentioning that the case of the structure tailoring provided possibilities to further optimize the properties of selenium-based materials with enormous potential for future multipurpose application.

ACKNOWLEDGMENTS

This work was supported by National Natural Science Foundation of China (21673300) and the Hubei Provincial Natural Science Foundation of China (2018CFB237, 2018CFB228).

REFERENCES

(1) Dunn, B., Kamath, H., Tarascon, J. M. Electrical Energy Storage for the Grid: A Battery of Choices. *Science* **2011**, 334, 928-935.

(2) Larcher, D., Tarascon, J. M. Towards Greener and More Sustainable Batteries for Electrical Energy Storage. *Nat. Chem.* **2015**, 7, 19-29.

(3) Chen, L.; Jiang, H.; Jiang, H. B.; Zhang, H. X.; Guo, S. J.; Li, C. Z.; Mo-Based Ultra Small Nanoparticles on Hierarchical Carbon Nanosheets for Superior Lithium Ion Storage and Hydrogen Generation Catalysis. *Adv. Energy Mater.* **2017**, 7, 1602782.

(4) Zhang, Y. F.; Zuo, L. Z.; Zhang, L. S.; Huang, Y. P.; Liu, T. X.; Cotton Wool Derived Carbon Fiber Aerogel Supported Few-Layered $MoSe_2$ Nanosheets as Efficient Electrocatalysts for Hydrogen Evolution. *ACS Appl. Mater. Interfaces.* **2016**, 8, 7077-7085.

(5) Yu, X. Y.; Lou, X. W.; Mixed Metal Sulfides for Electrochemical Energy Storage and Conversion. *Adv. Energy Mater*. **2018**, 8, 1701592.

(6) Ko, Y. N., Choi, S. H., Park, S. B., Kang, Y. C. Hierarchical $MoSe_2$ Yolk–Shell Microspheres with Superior Na-ion Storage Properties. *Nanoscale*, **2014**, 6(18), 10511-10515.

(7) Qu, B.; Yu, X. B.; Chen, Y. J.; Zhu, C. L.; Li, C. Y.; Yin, Z. X.; Zhang, X. T.; Ultrathin $MoSe_2$ Nanosheets Decorated on Carbon Fiber Cloth as Binder-Free and High-Performance Electrocatalyst for Hydrogen Evolution. *ACS Appl. Mater. Interfaces.* **2015**, 7, 14170-14175.

(8) Park, G. D.; Kim, J. H.; Park, S. K.; Kang,Y.C.; $MoSe_2$ Embedded CNT-Reduced Graphene Oxide Composite Microsphere with Superior Sodium Ion Storage and Electrocatalytic Hydrogen Evolution Performances. *ACS Appl. Mater. Interfaces*,**2017**, 9, 10673-10683.
(9) Zhu, M. N.; Luo, Z. G.; Pan, A. Q.; Yang, H. L.; Zhu, T.; N-Doped One-Dimensional Carbonaceous Backbones Supported $MoSe_2$ Nanosheets as Superior Electrodes for Energy Storage and Conversion. *Chem. Eng. J.* **2018**, 334, 2190-2200.
(10) Wang, H.; Wang, X.Y.; Wang, L.; Wang, J.; Jiang, D. L.; Li, G. P.; Zhang, Y.; Zhong, H. H.; Jiang, Y.; Phase Transition Mechanism and Electrochemical Properties of Nanocrystalline $MoSe_2$ as Anode Materials for the High Performance Lithium-ion Battery. *J. Phys. Chem. C* **2015**, 119, 10197-10205.
(11) Reddy, M. V.; Metal Oxides and Oxysalts as Anode Materials for Li Ion Batteries. *Chem. Rev.* **2013**, 113, 5364-5457.
(12) Shu, H. B.; Zhou, D.; Li, F.; Cao, D.; Chen, X. S.; Defect Engineering in $MoSe_2$ for The Hydrogen Evolution Reaction: From Point Defects to Edges. *ACS Appl. Mater. Interfaces.* **2017**, 9, 42688-42698.
(13) Liu, Y.; Zhu, M. Q.; Chen, D.; Sheet-Like $MoSe_2$/C Composites with Enhanced Li-ion Storage Properties. *J. Mater. Chem. A*, **2015**, 3, 11857-11862.
(14) Chia, X.; Eng, A. Y.; Ambrosi, A.; Tan, S. M.; Pumera, M.; Electrochemistry of Nanostructured Layered Transition-Metal Dichalcogenides, *Chem. Rev.* **2015**, 115, 11941-11966.
(15) Cong, L. N.; Xie, H. M.; Li, J. H.; Hierarchical Structures Based on Two-dimensional Nanomaterials for Rechargeable Lithium Batteries. *Adv. Energy Mater.* **2017**, 7, 1601906.
(16) Tang, W. J.; Xie, D.; Shen, T.; Wang, X. L.; Wang, D. H.; Zhang, X. Q.; Tu. J. P.; Construction of Nitrogen-Doped Carbon Coated $MoSe_2$ Microspheres with Enhanced Performance for Lithium Storage. *Chem. Eur. J.* **2017**, 23, 1-7.
(17) Wang, Y. W.; Yu, L.; Lou X. W.; Synthesis of Highly Uniform Molybdenum-Glycerate Spheres and Their Conversion into Hierarchical MoS_2 Hollow Nanospheres for Lithium-Ion Batteries. *Angew. Chem. Int. Ed*. **2016**, 55, 7423-7426.
(18) Yu, L.; Hu, H.; Wu, H. B.; Lou X. W.; Self-Templated Formation of Hollow Structures for Electrochemical Energy Applications. *Acc. Chem. Res.,* **2017**, 50, 293−301.
(19) Gu, F.; Li, C. Z.; Wang, S. F.; Lu, M. K. Solution-Phase Synthesis of Spherical Zinc Sulfide Nanostructures. *Langmuir* **2006**, 22, 1329-1332.
(20) Peng, Q.; Dong, Y. J.; Li, Y. D.; ZnSe Semiconductor Hollow Microspheres. *Angew. Chem. Int. Ed*. **2003,** 115, 3135-3138.
(21) Zhou, X.; Jiang, J.; Ding, T.; Zhang, J.; Yang, Q.; Fast Colloidal Synthesis of Scalable Mo-Rich Hierarchical Ultrathin $MoSe_{2-x}$ Nanosheets for High Performance Hydrogen Evolution. *Nanoscale* **2014**, 6, 11046-11051.
(22) Gao, D. Q.; Xia, B. R.; Zhu, C. R.; Du, Y. H.; Ding, J.; Activation of The $MoSe_2$ Basal Plane and Se-edge by B Doping for Enhanced Hydrogen Evolution. *J. Mater. Chem. A*, **2018**, 6, 510-515.
(23) Matte, H. S.; Plowman, S. R.; Datta, R.; Photoluminescence Emission and Raman Response of Monolayer MoS_2, $MoSe_2$, and WSe_2. *Dalton Trans*. **2011**, 40, 10322–10325.
(24) Ma, Q.; Isarraraz, M.; Wang, C. S.; Bartels, L.; Two-Dimensional Molybdenum Tungsten Diselenide Alloys: Photoluminescence, Raman Scattering, and Electrical Transport. *ACS nano,* **2014**, 8, 4672-4677.
(25) Huang, Y.; Xu, K.; Wang, Z.; Shifa, T. A.; He, J.; Designing the Shape Evolution of $SnSe_2$ Nanosheets and their optoelectronic properties, *Nanoscale* **2015**, 7, 17375-17380.
(26) Ithurria, S.; Tessier, M. D.; Mahler, B.; Lobo, R. P.; Dubertret, B.; Efros, A. L.; Colloidal Nanoplatelets with Two-Dimensional Electronic Structure. *Nat. Mater.* **2011**, 10, 936-941.
(27) Ithurria, S.; Dubertret, B.; Quasi 2D Colloidal CdSe Platelets with Thicknesses Controlled at the Atomic Level.

J. Am. Chem. Soc. **2008**, 130, 16504-16505.
(28) Huang, Y.; Xu, K.; Wang, Z.; Shifa,T. A.; He, J.; Designing the Shape Evolution of $SnSe_2$ Nanosheets and Their Optoelectronic Properties. *Nanoscale* **2015**, 7, 17375-17380.
(29) Chen, L.; Jiang, H.; Guo, S. J.; Li, C. Z.; Mo-Based Ultrasmall Nanoparticles on Hierarchical Carbon Nanosheets for Superior Lithium Ion Storage and Hydrogen Generation Catalysis. *Adv. Energy Mater*. **2017**, 7, 1602782.
(30) Wu, R.; Zhang, J. F.; Shi, Y. M.; Liu, D. L.; Zhang, B.; Metallic WO_2-Carbon Mesoporous Nanowires as Highly Efficient Electrocatalysts for Hydrogen Evolution Reaction. *J. Am. Chem. Soc.* **2015**, 137, 6983-6986.
(31) Wang, Y.; Ma, Z.; Chen, Y.; Zou, M.; Yousaf, M.; Yang, Y.; Yang, L.; Cao, A.; Han, R. P.; Controlled Synthesis of Core-Shell Carbon@MoS_2 Nanotube Sponges as High-Performance Battery Electrodes. *Adv. Mater*. **2016**, 28 10175-10181
(32) Wang, H.; Wang, X.Y.; Wang, L.; Wang, J.; Jiang, D.L.; Li, G.P.; Zhang, Y.; Zhong, H.H.; Jiang, Y.; Phase Transition Mechanism and Electrochemical Properties of Nanocrystalline $MoSe_2$ as Anode Materials for the High Performance Lithium-Ion Battery. *J. Phys. Chem. C* **2015**, 119, 10197–10205.
(33) Zheng, Y.; Zhou, T.; Zhang, C.; Mao, J.; Liu, H.; Guo, Z.; Boosted Charge Transfer in SnS/SnO_2 Heterostructures: Toward High Rate Capability for Sodium-Ion Batteries. *Angew. Chem. Int. Ed.* **2016**, 55, 3408-3413.
(34) Liu, S.N.; Cai, Z.Y.; Zhou, J.; Zhu, M. N.; Pan, A. Q.; Liang, S. Q.; High-Performance Sodium-Ion Batteries and Flexible Sodium-Ion Capacitors Based on Sb_2X_3 (X = O, S)/Carbon Fiber Cloth. J. *Mater. Chem. A* **2017**, 59169.
(35) Augustyn, V.; Come, J.; Lowe, M. A.; Kim, J.W.; Taberna, P. L.; Tolbert, S. H.; Abruña, H. D.; Simon, P.; Dunn, B.; High-Rate, Electrochemical Energy Storage Through Li^+ Intercalation Pseudocapacitance. *Nat. Mater.* **2013**, 12, 518-524.
(36) Kibsgaard, J.; Chen, Z. B.; Reinecke, B. N.; Jaramillo, T. F.; Engineering the Surface Structure of MoS_2 to Preferentially Expose Active Edge Sites for Electrocatalysis. *Nat. Mater.* **2012**, 11, 963−969.
(37) Merki, D.; Fierro, S.; Vrubel, H.; Hu, X. L.; Amorphous Molybdenum Sulfide Films as Catalysts for Electrochemical Hydrogen Production in Water. *Chem. Sci.* **2011**, 2, 1262−1267.
(38) Xie, J. F.; Zhang, H.; Li, S.; Lou, D.; Xie, Y.; Defect-Rich MoS_2 Ultrathin Nanosheets with Additional Active Edge Sites for Enhanced Electrocatalytic Hydrogen Evolution. *Adv. Mater*. **2013**, 25, 5807-5813.

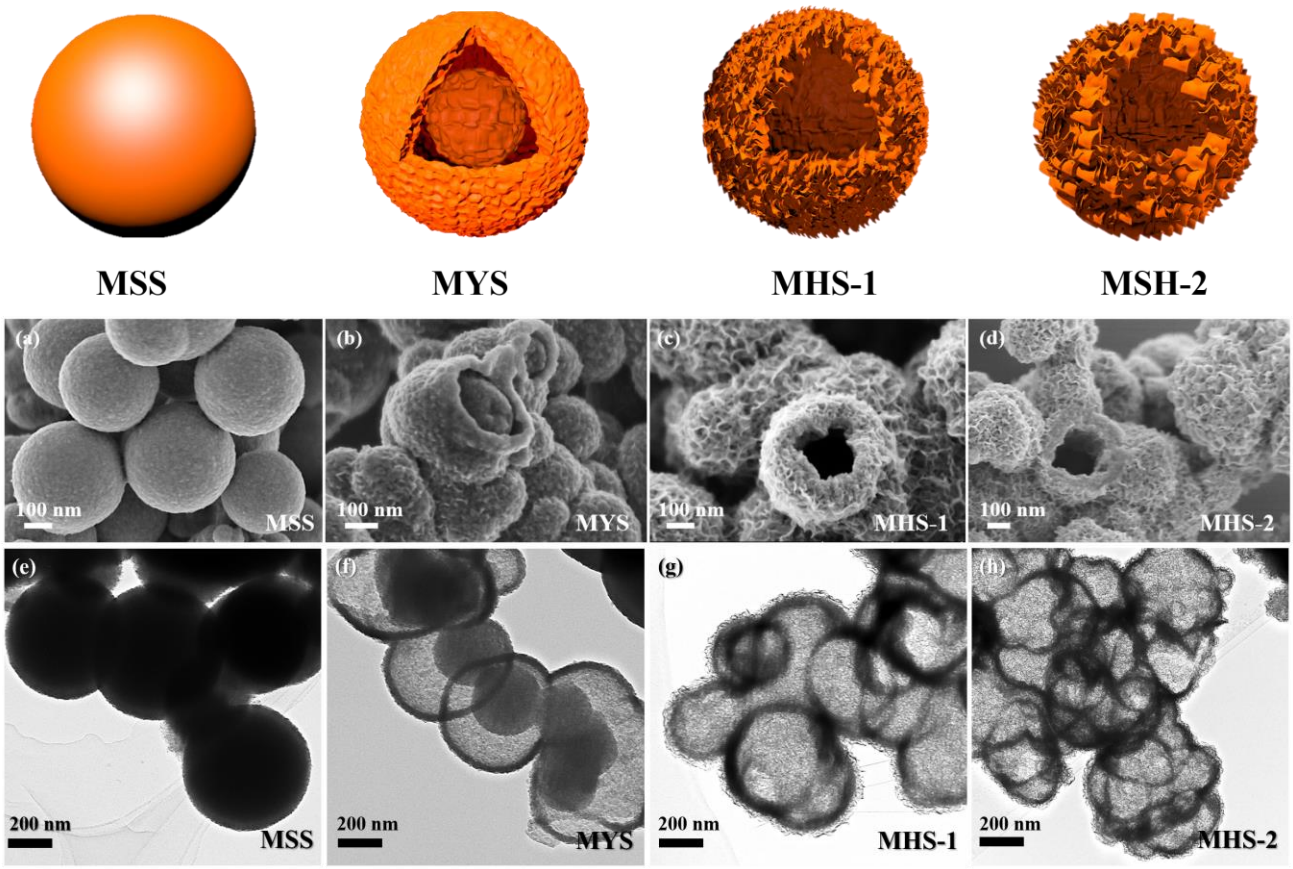

Figure 1. Illustration of the morphologies for $MoSe_2$ samples prepared at different temperatures. SEM and TEM images of $MoSe_2$ samples at different temperature (a, e) $MoSe_2$ solid nanospheres (MSS) 100 ℃, (b, f) $MoSe_2$ yolk-shell spheres (MYS) 140 ℃, (c, g) $MoSe_2$ hollow nanospheres (MHS-1) 180 ℃, (d, h) (MHS-2) 220 ℃.

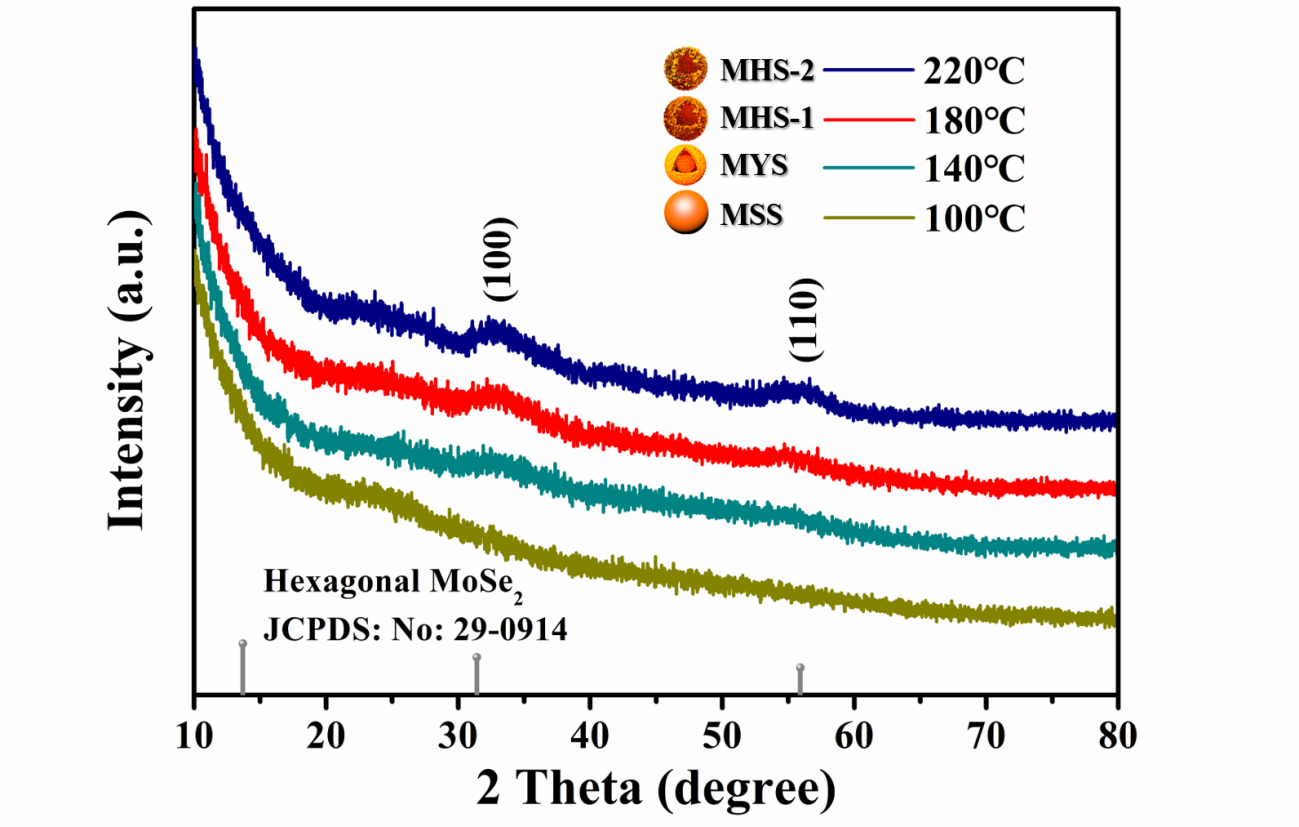

Figure 2. XRD patterns of the as synthesized $MoSe_2$ at different solvothermal temperature. $MoSe_2$ solid nanospheres (MSS) 100 ℃, $MoSe_2$ yolk-shell spheres (MYS) 140 ℃, $MoSe_2$ hollow nanospheres (MHS-1) 180 ℃, (MHS-2) 220 ℃.

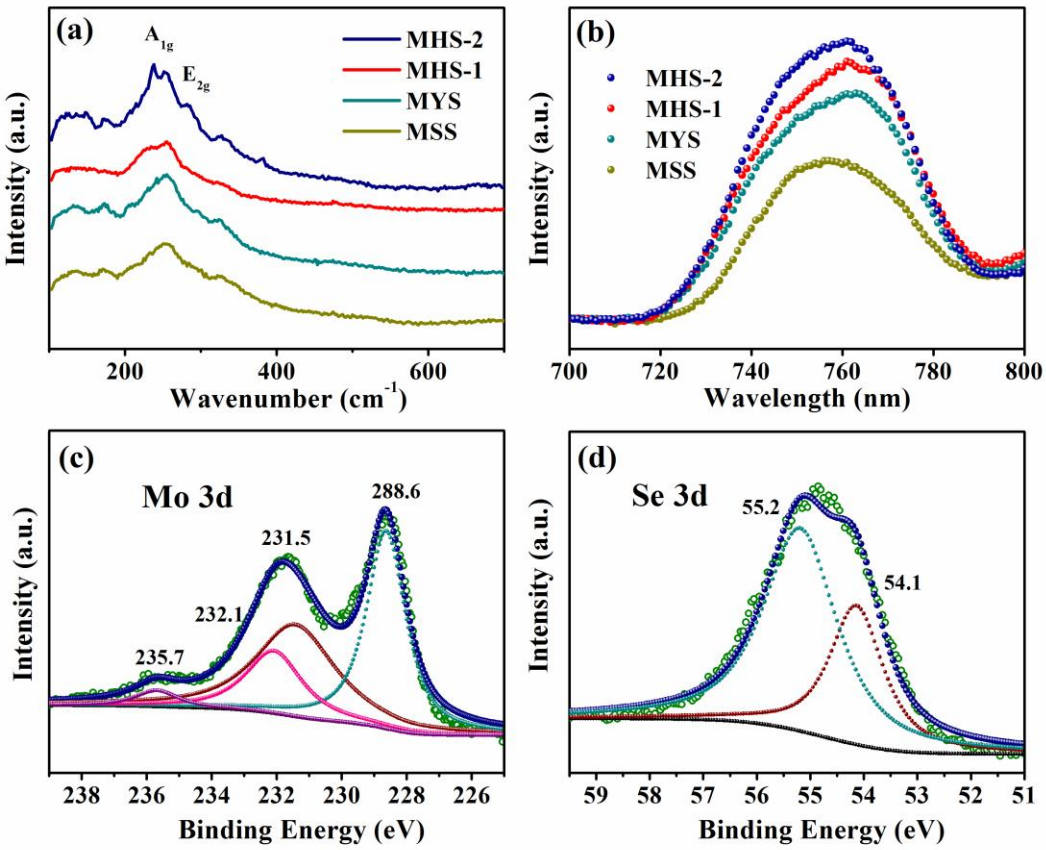

Figure 3. (a) Raman spectra, (b) PL spectra of $MoSe_2$ samples. (c, d) XPS results of MHS-1.

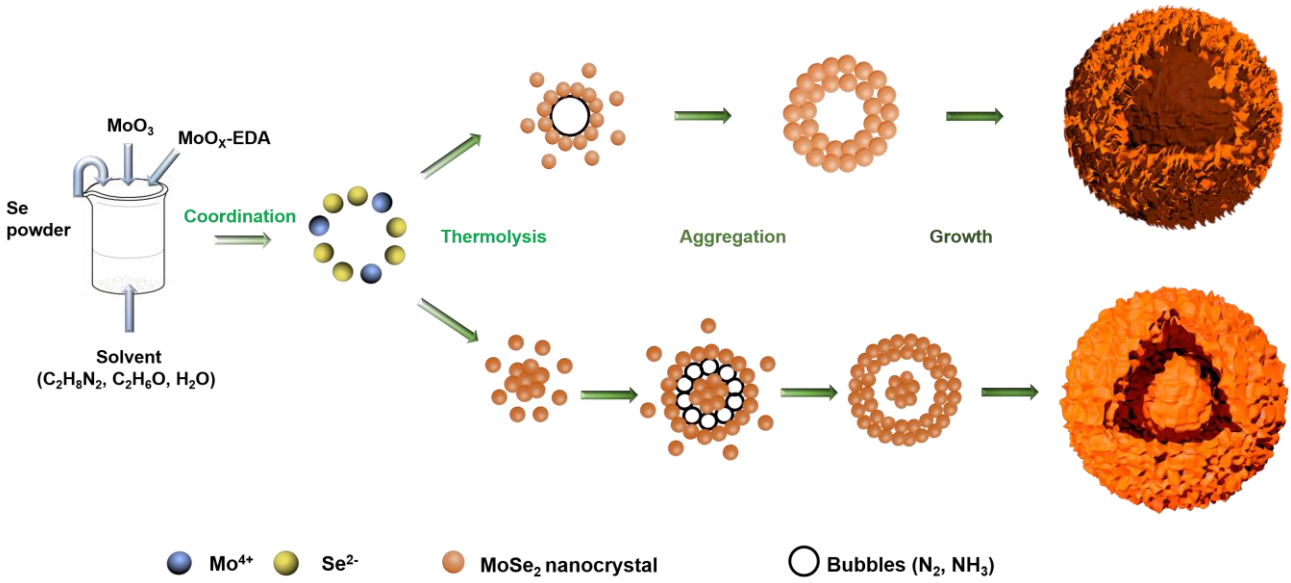

Scheme 1. Illustration of the $MoSe_2$ Yolk-shell and Hollow Nanospheres Formation.

Table 1: BET surface area and HER performances of $MoSe_2$ samples.

Sample	S_{BET} (m^2 g^{-1})	Tafel slope (mV/dec)	Onset η/mV
MSS	2.1	102	200
MYS	17.9	80	170
MHS-1	66.5	58.9	150
MHS-2	41.9	68.5	190

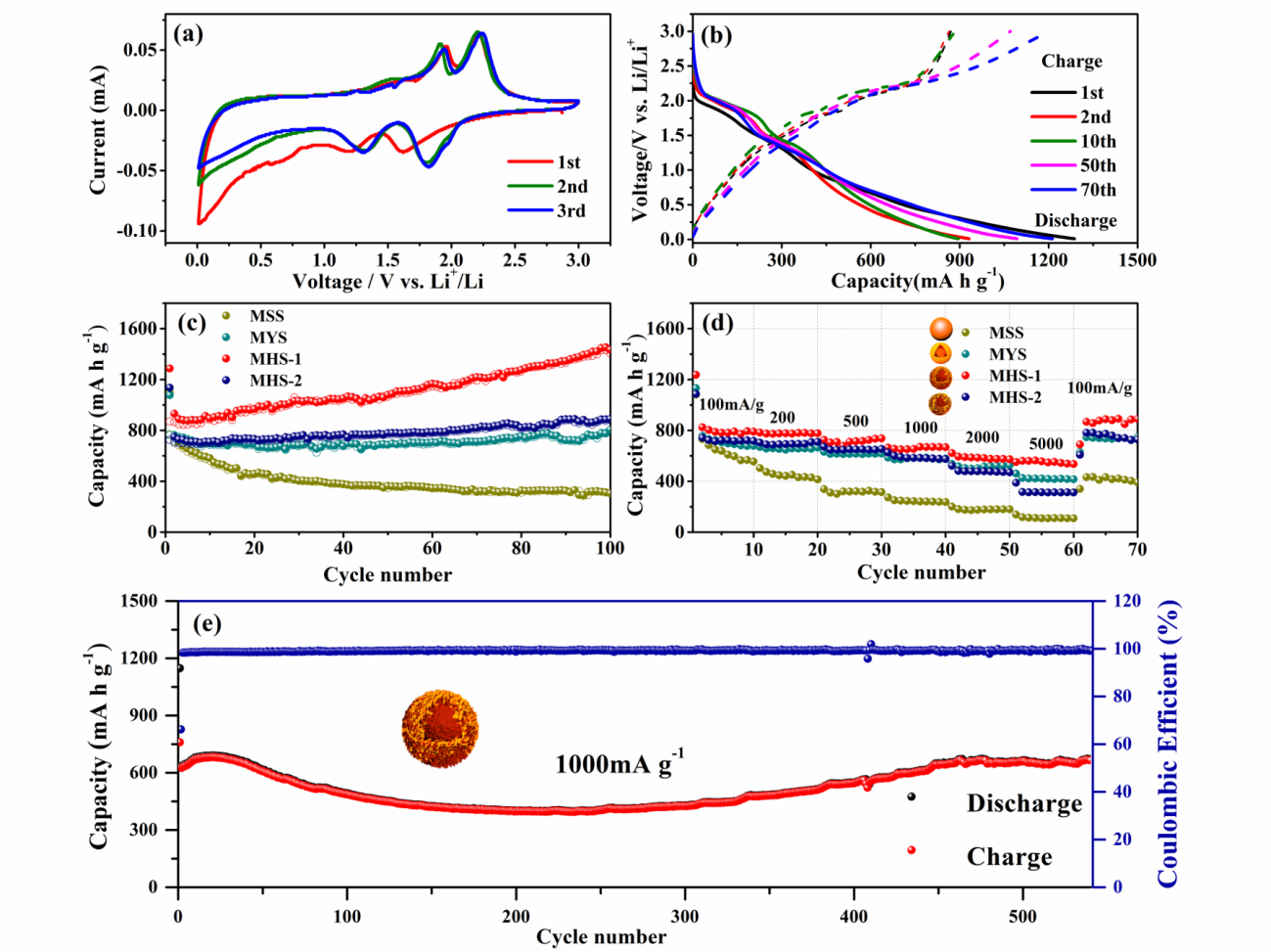

Figure 4. (a) CV curves of MHS-1 at 0.1 mV s^{-1}, (b) GCD curves of MHS-1 for 1st, 2nd, 10th, 50th, and 70th cycle at 100 mA g^{-1}, (c) rate performances of $MoSe_2$ samples at current densities of 100, 200, 500, 1000, 2000 and 5000 mA g^{-1}, (d) cycling performances of $MoSe_2$ samples at 100 mA g^{-1}, (e) long-term cycling performances of MHS-1 at 1.0 A g^{-1}.

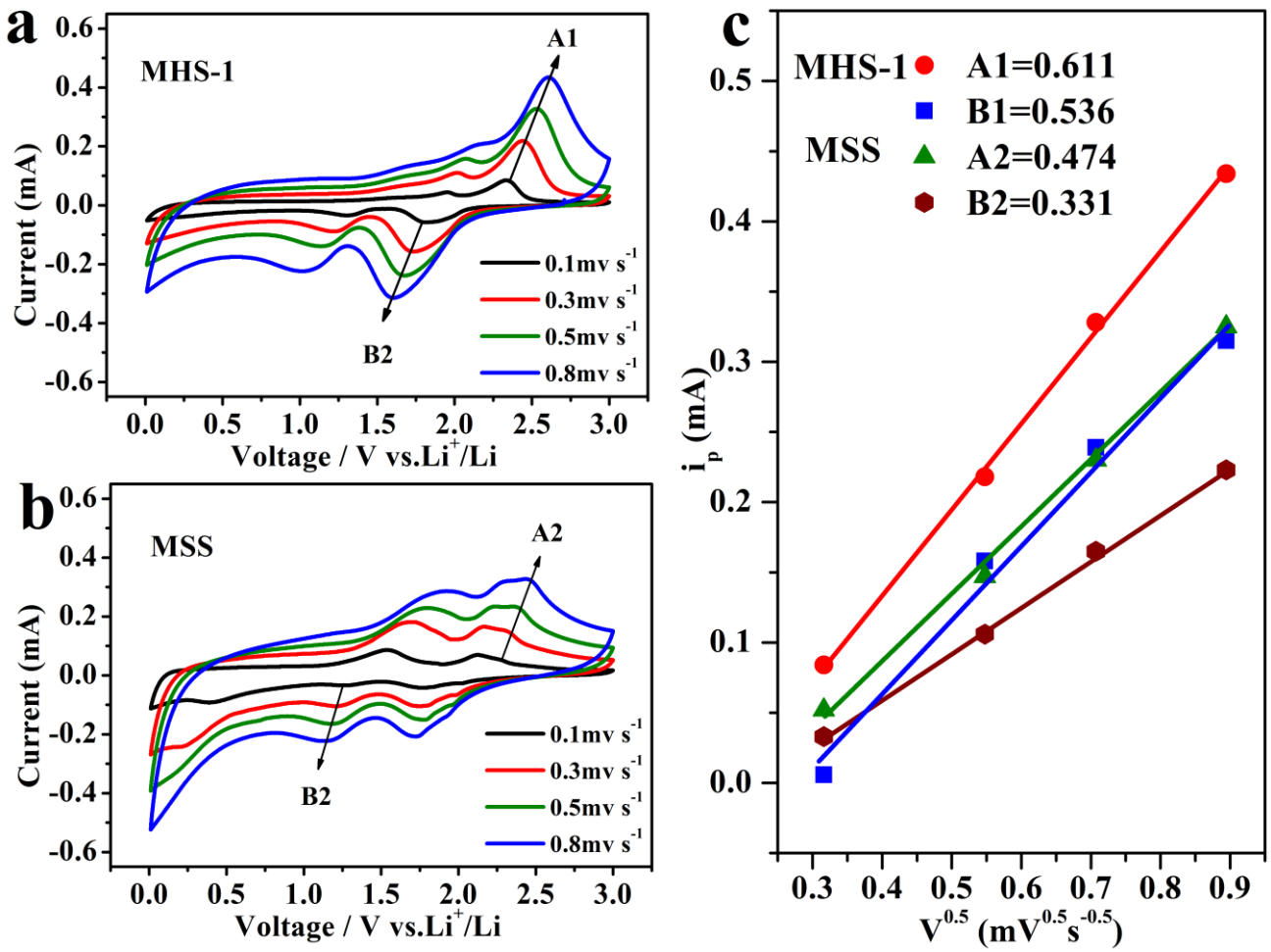

Figure 5. (a) CV scans at various sweep rates for LIB cells with (a), MHS-1, and (b), MSS electrodes, (c) the obtained *A* values with the $i_p = Av^{1/2}$ relationship.

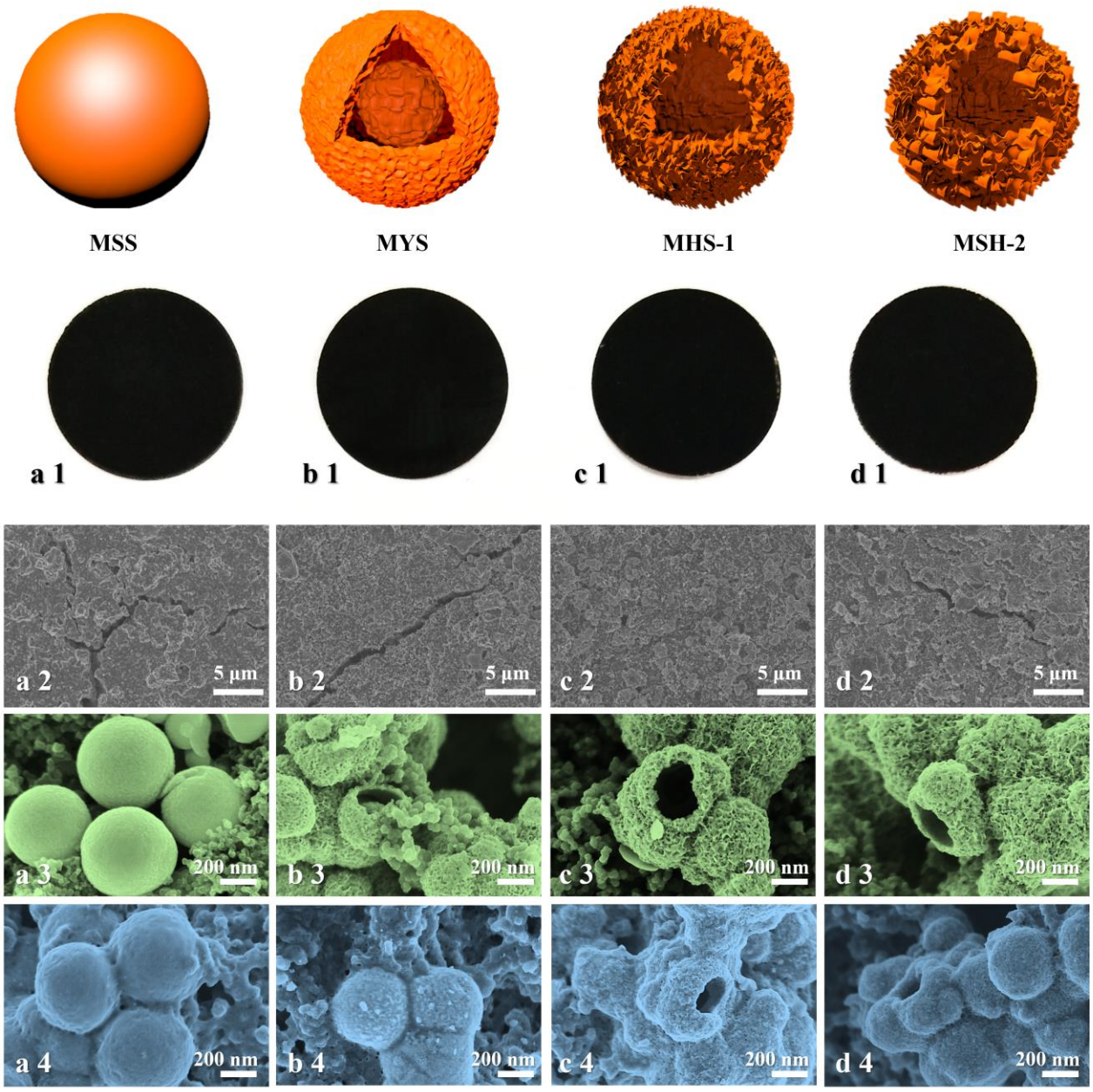

Figure 6. Electrode surface morphologies. Digital camera photos (a1-d1) and SEM images (a2-d2) of surface morphology of electrodes after 10 cycles. Typical SEM images of $MoSe_2$ electrodes before (a3-d3) and after (a4-d4) 10 cycles at the current density of 200 mA g^{-1}.

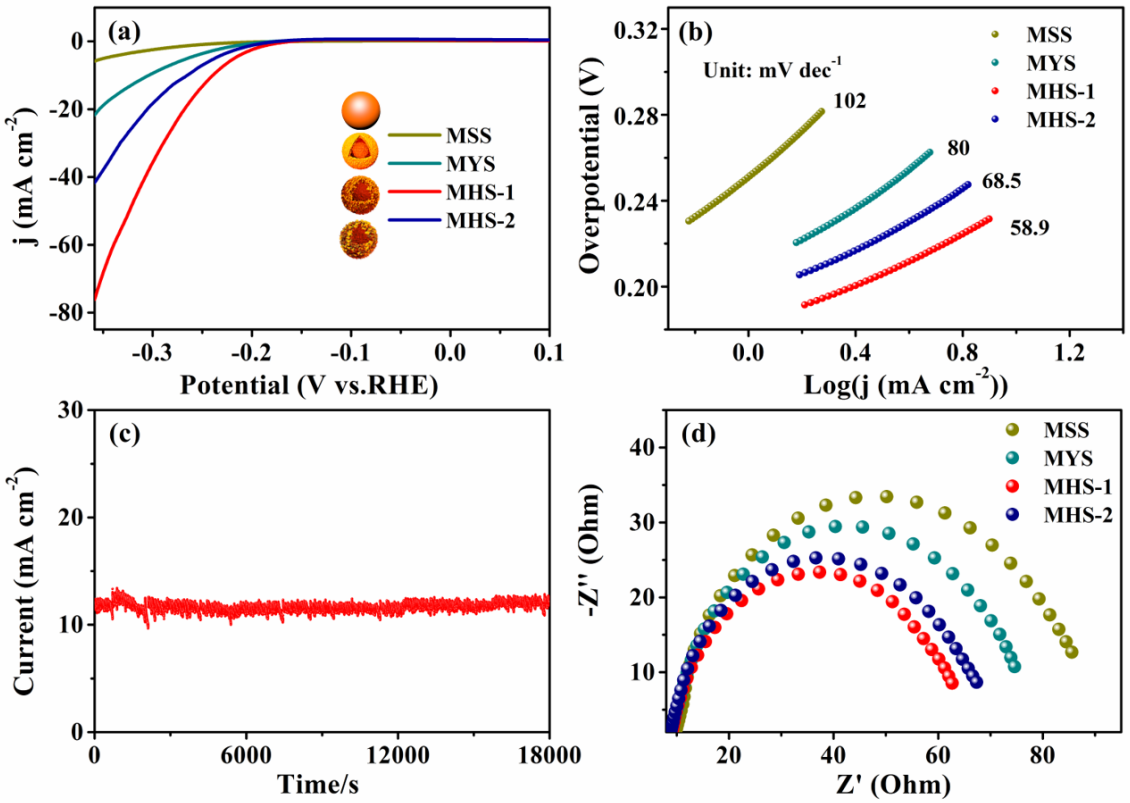

Figure 7. (a) Polarization curves, (b) Tafel plots, (d) EIS of $MoSe_2$ samples, (c) Cycling stability of MHS-1 at an overpotential of 230 mV.

TOC

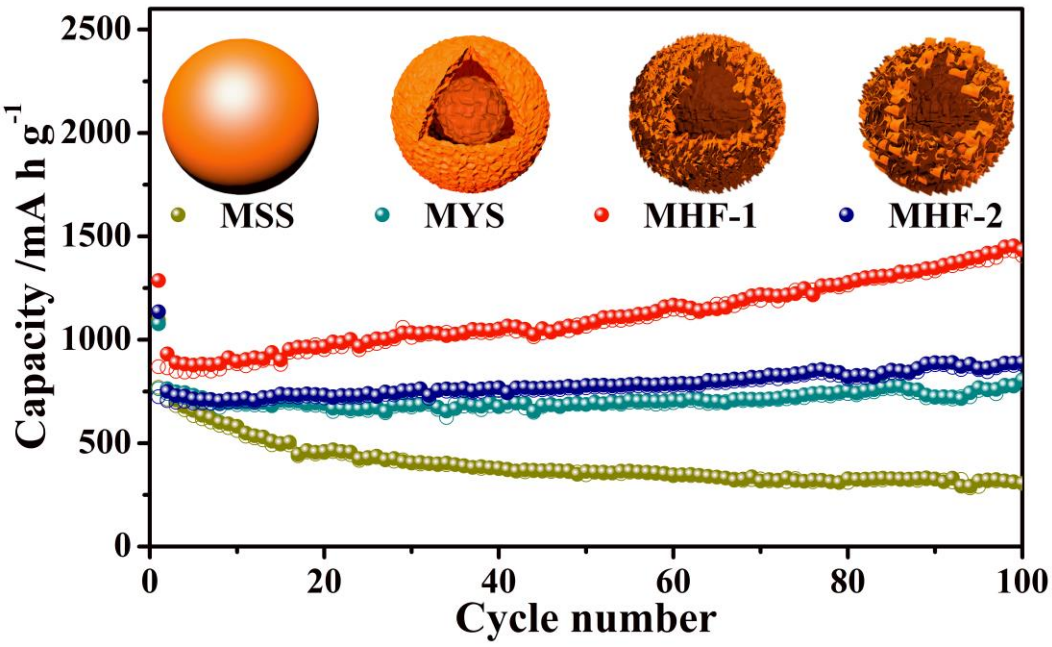
2500
2000
1500
1000
500
0
Capacity /mA h g-1
MSS
MYS
MHF-1
MHF-2
0
20
40
60
80
100
Cycle number